



Does the thermal conductivity of gas diffusion layer matter in polymer electrolyte fuel cells?

Christoph Csoklich^a, Mayank Sabharwal^a, Thomas J. Schmidt^{a,b}, Felix N. Büchi^{a,*}

^a Electrochemistry Laboratory, Paul Scherrer Institut, Forschungsstrasse 111, Villigen PSI, 5232, Switzerland

^b Laboratory of Physical Chemistry, ETH Zürich, Vladimir-Prelog-Weg 1-5/10, Zurich, 8093, Switzerland

HIGHLIGHTS

- Studied the effect of fiber thermal conductivity using GDLs with identical micro-structure.
- Investigation of the water and heat transport by thermal modeling and experiments.
- Two-layered GDLs outperform carbon GDLs regardless of their thermal conductivity.

ARTICLE INFO

Keywords:

Polymer electrolyte fuel cell
Gas diffusion layer
Water management
Thermal conductivity
Ordered microstructure
Deterministic transport

ABSTRACT

Water management is a highly critical parameter for improving the performance of polymer electrolyte fuel cells (PEFCs) at high current densities. The microstructure and properties of the gas diffusion layer (GDL) play an important role in the distribution of the reactant gases and drainage of the liquid water produced in the catalyst layer during PEFC operation. In this context, the community still debates on the role and optimum values of the GDL's thermal conductivity and if it is even the decisive factor for water management. This study presents insight into this fundamental question by reporting experimental performance and thermal modeling data of GDLs with identical, ordered microstructure but different thermal conductivities. Results show that lower GDL thermal conductivity produces higher temperature gradients in the GDL, which are, however, partially compensated by a heat pipe cooling mechanism. Even with an order of magnitude different thermal conductivity, the ordered, deterministic GDLs surpass the performance of a conventional carbon GDL. Our findings suggest that the thermal conductivity should not be a decisive criterion for future materials developments of optimized GDLs to improve fuel cell performance at high current densities, but rather the GDL structure.

1. Introduction

Polymer electrolyte fuel cells (PEFCs) technology offers a high gas to power conversion efficiency and power density, making it suitable for both mobile and stationary applications [1–6]. The high system cost per installed power is dominated by material costs of precious metal platinum catalysts or corrosion-resistant bipolar plates and thus, limits their current market share [7,8]. To reduce cost, both power density and conversion efficiency have to be increased. The performance and cost targets, set up by the U.S. Department of Energy and the New Energy and Industrial Development Organization of Japan (NEDO) to tackle this challenge, can only be achieved with the use of advanced functional materials [9–13].

Fuel cell performance is limited by three major loss mechanisms. Activation losses, caused mainly by the sluggish reaction kinetics of the

oxygen reduction reaction (ORR), significantly reduce the conversion efficiency and are dominant at low current densities [14,15]. Ohmic losses, due to contact, through-plane, and protonic resistances, reduce the cell voltage linearly with increasing current density [16]. Finally, mass transport losses dominate and limit the performance at high current densities (with high water production), where oxygen transport to the cathode catalyst layer is limiting. At these conditions, product water accumulates in the pores of the cathode catalyst layer (CL) and GDL and blocks the gas pathways, decreasing the effective gas diffusivity [17].

In state-of-the-art PEFCs, the GDL is a combination of a macroporous GDL and micro-porous layer (MPL), which provide a hierarchical pore size distribution [18,19]. Conventional GDL are carbon papers or felts, made from carbon fibers with a diameter of few microns. They are

* Corresponding author.

E-mail address: felix.buechi@psi.ch (F.N. Büchi).

highly porous (around 75%), between 140 μm to 200 μm thick and have a typical median pore size of around 30 μm [20]. The MPL is a micro-to nano-porous pore structure, coated onto the GDL and in contact with the CL. It is made of carbon nanoparticles and a fluoropolymer binder and is around 30 μm to 50 μm thick. Efficient water management, i.e., removal of liquid water produced by the ORR while maintaining high gas transport to the CL and a sufficiently humidified membrane, is a critical factor influencing the design of these layers.

An ideal GDL would drain liquid water directly from the CL to the channel. However, conventional GDLs are random and heterogeneous resulting in a stochastic pore and throat network, where liquid water is transported via capillary fingering [21]. Following the path of least resistance, water transport through the GDL might be highly tortuous resulting in a high in-plane saturation which impedes the gas transport to the CL [22,23]. Many approaches to direct water on its way through the GDL have been investigated in the past, but also the limits of modifications to conventional GDLs have been reported recently [24–26]. In our previous work, we demonstrated the potential of fully deterministic GDL fabrics with an ordered microstructure which facilitates efficient water transport at all conditions, leading to a significant reduction in the mass transport overpotentials compared to current state-of-the-art conventional GDLs [27]. The thermal conductivity of the GDL is tightly connected with its water transport properties, as the temperature distribution inside the structure influences the local water vapor saturation pressure and interphase mass transfer [28]. Carbon fibers provide common GDLs with a reasonably good thermal conductivity, which is anisotropic in in-plane and through-plane directions, depending on the predominant fiber orientation, determined by the manufacturing process. Thus, differences in thermal conductivity were always coupled to a different GDL structure and an independent analysis of the impact of the thermal conductivity was impeded. Therefore, it has been difficult to understand the effect of the GDL thermal conductivity and consequently, determination of an optimum value for it.

This work aims to provide a fundamental understanding of the impact of the thermal conductivity on water management and cell performance. A novel set of GDLs, prepared with different thermal conductivities while conserving its pore and fiber structure, are used to probe the effect of the thermal conductivity on the water and heat transport. To the best of our knowledge, this is the first time such a controlled parametric study is performed. The GDLs are manufactured with woven polyethylene terephthalate (PET) fabrics which are sputter-coated with two different thicknesses of gold. The gold coating provides the fabric with the required electronic and thermal properties. While the electronic conductivities are comparable or better than a conventional Toray carbon paper, the thermal conductivities are 1–2 orders of magnitude lower. Electrochemical measurements, oxygen transport resistance characterization, and 2D thermal model calculations are used to elucidate the influence of the thermal conductivity of GDLs on water management and cell performance. The results can provide design guidelines with respect to the thermal properties for future GDL developments.

2. Experimental

2.1. Material characterization

S-PET is a two-layered PET fabric (provided by Sefar AG, Switzerland). Its weaving properties are listed in Table 1. The plain PET fabric was sputtered with gold to render it electronically and thermally conductive, necessary for fuel cell application. EDX analysis was carried out to confirm the presence of gold and was presented in a previous publication [27]. The approach uniquely allows to tune the thermal and electrical properties while maintaining the identical GDL structure. Therefore, S-PET GDLs are a powerful model system to separate the

Table 1

| Structural GDL properties of S-PET and T60. | | |
|---------------------------------------------|------------------|--------------|
| Material | S-PET | T60 |
| Fiber \varnothing [μm] | 80 | ≈ 10 |
| | 24 | |
| Density [cm^{-3}] | 31×40 | |
| | 190×240 | |
| Thickness [μm] | 180 | 190 |
| compressed | 170 | 170 |

influence of micro-structure and thermal conductivity on water management. For economically viable and durable woven GDLs, weaving of conductive fibers or sputtering with cheaper elements such as silver or even carbon seem promising.

Two thicknesses of 100 nm and 500 nm were selected to set effective conductivities ca. an order of magnitude apart. Bulk in-plane and through-plane electronic conductivities were measured with two separate four-point-probe setups. For measuring the through-plane conductivity the same setup was used as described in a previous publication [27]. The in-plane conductivity σ_{ip} was measured on 1.5 cm \times 5 cm large samples, which were clamped between gold-coated copper current collectors. Two retractable gold pins with a separation distance of 10 mm were gently lowered onto the surface and the voltage drop was measured repeatedly for different positions at a current of 0.1 A. The retractable pins ensured the same contact pressure for each measurement and sample.

From the values of the electronic conductivity the thermal conductivity was calculated using the Wiedemann–Franz law: [29]

$$\kappa = \sigma \cdot T \cdot 2.44 \times 10^{-8} \text{ W } \Omega \text{ K}^{-2} \quad (2.1)$$

The resulting conductivity values $\kappa_{ip/tp}$ correspond to the electronic contribution to heat transfer (referred to as Au-100/Au-500). The total thermal conductivity of the gold-coated composite materials (of S-PET-1/5) should however comprise also the contribution from the PET backbone structure. This was simulated with the ConductoDict module of the commercial GeoDict® software (Math2Market, Germany), using the real woven structure, gained from XTM scans, as simulation input. Symmetric temperature boundary conditions were chosen on opposing sides of the structure and the PET bulk thermal conductivity ($0.24 \text{ W m}^{-1} \text{ K}^{-1}$) was used for the simulation.

2.2. Fuel cell performance analysis

2.2.1. MEA and cell assembly

All GDL materials (S-PET-1, S-PET-5, T60) were tested in a differential fuel cell with an active area of 5 cm^2 . The active area of 2 cm \times 2.5 cm was set with two 25 μm thick PEN subgaskets which were hot-pressed onto both sides of a 15 μm thick Gore® Primea® catalyst coated membrane (A510.1/M815.15/C510.4 - An., Cath. 0.1 mgPt/ cm^2 , 0.4 mgPt/ cm^2). Symmetric graphite flow fields (Diabon NS2) were used with channel and land widths of 0.4 mm and a channel depth of 0.5 mm. This adaption was chosen from previous X-ray tomographic microscopy (XTM) findings, that showed water accumulation in large pores of the carrier mesh below a flow field rib [27]. The fraction of totally enclosed pores (300 μm width) was thereby significantly reduced with the thinner flow field ribs (400 μm).

The GDL materials were symmetrically assembled between polymer gaskets on the anode and cathode sides. GDL compression was calculated with the use of 175 μm thick PTFE and FEP gaskets to 10%, following the procedure of Simon et al. [30]. The whole MEA was held in place with alignment pins between the flow fields and compressed with 10 M8 bolts through the end-plates (5 N m torque).

Table 2
Material properties and cell design parameters.

| Description | Value |
|--------------------------------------------------|---------------------------|
| S-PET-X thickness, d_{SPET} | 180 μm |
| T60 thickness, d_{T60} | 190 \pm 5 μm |
| Catalyst coated membrane thickness, d_{CCM} | 35 μm |
| Membrane Thickness (Gore Primea M815), d_{Mem} | 15 μm |
| Anode catalyst layer thickness, d_{aCL} | 4 μm |
| Cathode catalyst layer thickness, d_{cCL} | 16 μm |
| Channel/Land width, w_{rib} | 0.4 mm |
| Channel depth, d_{ch} | 0.5 mm |
| Active area, A_{act} | 5 cm^2 |
| Operating temperature, T_{op} | 50 °C/80 °C |
| Operating Pressure, p_{op} | 150 kPa |

2.2.2. Fuel cell operation

All assembled fuel cells (at least two per GDL material) were conditioned on an in-house built test bench before the experiments. This procedure was conducted at 80 °C under full gas humidification, gas pressure of 150 kPa and gas flow rates of 1.5 NL/min H_2 and air with a voltage step cycle between 0.95 V–0.6 V for about 8 h, following previous studies [27].

During the polarization curve experiments, the anode gas humidity (RH_A) was kept at a constant 80%, relative to the live monitored flow field temperature. Cathode gas humidity (RH_C) was varied between 60% for dry conditions and 100% for saturated conditions, to simulate different humidity conditions present in a fuel cell stack. A more comprehensive metric for the presented results is the dew-point. Therefore, the “dry” reference case corresponds to dew points of 74.6 °C/67.8 °C, and the “saturated”/“wet” case to 74.6 °C/80 °C on anode/cathode sides.

The polarization curves were recorded by setting galvanostatic steps of 25–100 mA cm^{-2} , lasting 30 s ($\leq 200 \text{ mA cm}^{-2}$) or 3 min ($> 200 \text{ mA cm}^{-2}$), until the cell voltage fell below 0.45 V. For each step, the cell voltage was averaged over the last third of the step and data points recorded at 1 Hz. The given error bars indicate cell to cell variations.

2.2.3. Limiting current analysis

Limiting current was measured for varying oxygen dilutions from 1%–60% at 50 °C and 80 °C, and “dry” and “saturated” conditions. For these measurements, the humidity was slightly adjusted to ensure stable operating conditions. Therefore, dewpoints of the dry case were symmetrically 67.8 °C, whereas for the wet case the set RH_C was lowered by 5% to 95%, corresponding to dew points of 74.6 °C/78.7 °C for anode/cathode side (or 80%/95% RH_A/RH_C). The cell voltage was ramped down from 300 mV to 50 mV. The value for the limiting current was determined depending on the dry current oxygen concentration $x_{\text{O}_2, \text{dry}}$, following the method described by Simon et al. The oxygen transport resistance related to the limiting current was calculated with the following Equation:

$$R_{T, \text{O}_2} = \frac{4F}{R \cdot T_{\text{cell}}} \cdot \frac{(p_{\text{abs}} - p_{\text{H}_2\text{O}})}{j_{\text{lim}}} \cdot x_{\text{O}_2, \text{dry}} \quad (2.2)$$

2.3. Thermal modeling

2.3.1. Simulation parameters

The thermal conductivity in in-plane and through-plane directions was measured for S-PET-1 and S-PET 5, and literature values are taken for T60, the catalyst layers, and the membrane. The used input values are summarized in Tables 2 and 3, and can be found in Figure S2.

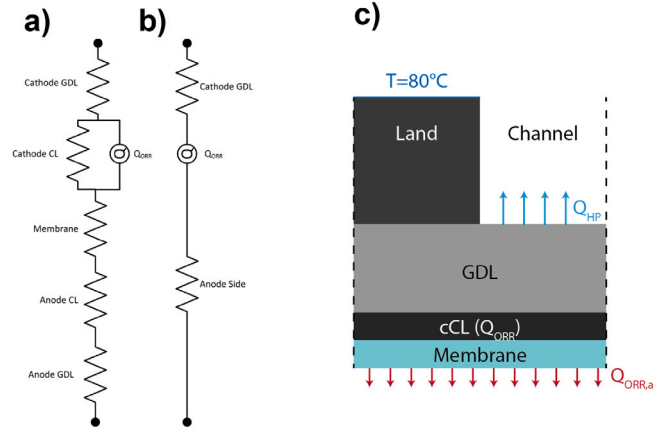


Fig. 1. (a–b) 1D equivalent circuit of heat production (Q_{ORR}) in the cathode catalyst layer and the adjacent thermal resistances from the membrane, catalyst layer, and GDLs. (c) Illustration of the model setup, simulation domain, and the used boundary conditions.

2.3.2. Model setup and boundary conditions

The 2D model uses Fourier’s law in steady-state with the known thermal conductivity values κ_{ip}/t_p and geometrical parameters of all components. The thermal balance is shown in cf. Eq. (2.3) where \mathbf{S} indicates a volumetric heat source term. The heat production Q_{ORR} in the cathode catalyst layer was approximated as 870 mW cm^{-2} (at a current density of 1.5 A cm^{-2}). The volumetric heat source term in Eq. (2.3) was set to $870 \text{ mW cm}^{-2}/d_{cCL}$ and assumed to be zero everywhere else in the domain. The heat produced by the ORR flows not only to the cathode side, but partially through the membrane to the anode flow field, which was included as a flux boundary at the membrane/aCL interface.

$$\nabla \cdot \mathbf{q} = -\nabla \cdot \kappa \nabla T = \mathbf{S} \quad (2.3)$$

$$\kappa = \begin{pmatrix} \kappa_{ip} & 0 \\ 0 & \kappa_{tp} \end{pmatrix} \quad (2.4)$$

With decreasing thermal conductivity of the GDL, the relative contribution from the membrane resistance drops, and therefore a higher percentage of the waste heat can flow to the anode (cf. Figure S3). For S-PET-1 (lowest thermal conductivity κ_{ip}), this results in a close to 50%/50% distribution of heat flux to anode and cathode sides, whereas for T60 more than 60% flow to the cathode flow field. The equivalent circuit used to model the thermal resistances in the cell is presented in Fig. 1 a-b. The thermal resistances of all components were calculated following Eq. (2.5)–(2.8). The effective heat flux $Q_{\text{ORR},a/c}$ to the anode and cathode sides was calculated with Eq. (2.9).

$$R_{th,i} = \frac{A}{\kappa_i \cdot d_i} \quad (2.5)$$

$$R_{th,c} = R_{cGDL} \quad (2.6)$$

$$R_{th,a} = R_{th,aGDL} + R_{th,aCL} + R_{th,Mem} \quad (2.7)$$

$$R_{th,total} = \frac{R_{th,a} \cdot R_{th,c}}{R_{th,a} + R_{th,c}} \quad (2.8)$$

$$Q_{\text{ORR},a} = \frac{Q_{\text{ORR}} \cdot R_{th,c}}{R_{th,a} + R_{th,c}} = Q_{\text{ORR}} - Q_{\text{ORR},c} \quad (2.9)$$

The simulation domain comprised of a half channel–half land domain and included the membrane, cathode CL, GDL and land. The channel is not simulated in the domain and only the GDL–channel and land–channel boundaries are considered. The boundary conditions for the problem are illustrated in Fig. 1 c. A constant temperature at the land ceiling of 80 °C was assumed. Symmetry boundary conditions (no flux) were assumed at the outer walls of the domain. A no flux boundary condition was assumed between the land and channel assuming a local thermal equilibrium. Depending on the previously calculated relative

Table 3
Transport and thermal properties of fuel cell components.

| Description | Reference | Value |
|----------------------------------------------------------------------|------------------------|-----------------------------------------|
| S-PET-1 in-plane electronic conductivity, $\sigma_{ip,SPET1}$ | Exp. | 1800 S m ⁻¹ |
| S-PET-1 through-plane electronic conductivity, $\sigma_{tp,SPET1}$ | Exp. | 550 S m ⁻¹ |
| S-PET-5 in-plane electronic conductivity, $\sigma_{ip,SPET5}$ | Exp. | 16 000 S m ⁻¹ |
| S-PET-5 through-plane electronic conductivity, $\sigma_{tp,SPET5}$ | Exp. | 55 000 S m ⁻¹ |
| T60 in-plane electronic conductivity, $\sigma_{ip,T60}$ | Zamel et al. [31,32] | 15 000 S m ⁻¹ |
| T60 through-plane electronic conductivity, $\sigma_{tp,T60}$ | Zamel et al. [31,32] | 1200 S m ⁻¹ |
| S-PET-1 in-plane thermal conductivity, $\kappa_{ip,SPET1}$ | Exp. | 0.057 W m ⁻¹ K ⁻¹ |
| S-PET-1 through-plane thermal conductivity, $\kappa_{tp,SPET1}$ | Exp. | 0.084 W m ⁻¹ K ⁻¹ |
| S-PET-5 in-plane thermal conductivity, $\kappa_{ip,SPET5}$ | Exp. | 0.2 W m ⁻¹ K ⁻¹ |
| S-PET-5 through-plane thermal conductivity, $\kappa_{tp,SPET5}$ | Exp. | 0.52 W m ⁻¹ K ⁻¹ |
| T60 in-plane thermal conductivity, $\kappa_{ip,T60}$ | Zamel et al. [33] | 12 W m ⁻¹ K ⁻¹ |
| T60 through-plane thermal conductivity, $\kappa_{tp,T60}$ | Zamel et al. [34] | 1.4 W m ⁻¹ K ⁻¹ |
| Membrane electronic conductivity, σ_{mem} | Manufacturer | 3.7–12 S m ⁻¹ |
| Membrane thermal conductivity, κ_{mem} | Pharoah et al. [35,36] | 0.2 W m ⁻¹ K ⁻¹ |
| An./cath. catalyst layer electronic conductivity, σ_{CL} | Sinha et al. [37,38] | 200 S m ⁻¹ |
| An./cath. catalyst layer thermal conductivity, κ_{CL} | Khandelwal et al. [36] | 0.27 W m ⁻¹ K ⁻¹ |
| Flow field thermal conductivity, κ_{ff} | Manufacturer | 90 W m ⁻¹ K ⁻¹ |
| Contact resistance contribution, R_{CR} | Makharia et al. [16] | 16.4 mΩ cm ² |
| Reaction waste heat at 1.5 A cm ⁻² , Q_{th} | estimated | 870 mW cm ⁻² |
| Maximum heat pipe cooling power at 1.5 A cm ⁻² , Q_{HP} | estimated | 320 mW cm ⁻² |

flux to the anode and cathode side, a Neumann boundary condition was set at the membrane/anode catalyst layer interface side with a heat flux of $Q_{ORR,a}$.

In the first simulation set (case 0), no heat pipe was considered, and all heat was transferred to the flow field rib only. This means that Q_{HP} is zero in this case. In the other case (case 1), the additional heat pipe flux of 320 mW cm⁻² was implemented at the GDL/channel interface. This heat flux was calculated by assuming full evaporation of product water, which is produced at 1.5 A cm⁻² with a heat of vaporization of 2.3 kJ g⁻¹. The anisotropic thermal conductivity of all GDLs was considered (cf. Eq. (2.4)).

The model was discretized using finite difference method and implemented in a python script. The mesh consisted of a grid with 200 × 100 cells for the GDL domain, 200 × 60 cells for both cCL and membrane and 100 × 50 cells for the land. The corresponding temperature distributions for membrane, cCL, GDL, and the land were extracted and plotted. The average, minimum and maximum values of the single components for each material and simulation case are summarized in Table S1.

2.3.3. HFR analysis

The high frequency resistance (HFR) was measured across the entire fuel cell assembly between the graphite flow fields (FF) with a Tsuruga E3566 AC milliohm meter (Tsuruga Electric Co., Japan) at 1 kHz. Therefore it contains contributions from contact resistances (FF/GDL, GDL/CL, CL/Membrane), electronic bulk resistances (GDLs, CLs, Membrane) and the proton resistance of the membrane. The HFR of all three materials was extracted at 1.5 A cm⁻². For T60, which did not reach this current density in saturated conditions, the HFR value was chosen at the highest current density before the mass transport related voltage drop occurred. Membrane conductivity was calculated for varying RH from manufacturer data. With the measured (GDL bulk resistance) and literature values (contact resistance) the total HFR was calculated by adding the single contributions.

3. Results and discussion

3.1. Material characterization and thermal conductivity tuning

For having different thermal conductivities but identical gas diffusion layer (GDL) structure, a base material consisting of a two-layered,

woven PET fabric (referred to as S-PET) with an overall thickness of 180 μm was used. The fabric consists of a fine surface layer (fiber-Ø 24 μm) and a coarse carrier structure (fiber-Ø 80 μm). The material was sputtered with gold with thicknesses of 100 nm and 500 nm (cf. Fig. 2). These gold-coated S-PET materials are referred to as S-PET-1 and S-PET-5. More details on the structure and water transport mechanism through this material have been described in our previous work [27]. With this approach, the GDL structure and its electronic and thermal conductivities can be separated and the conductivities altered independently. All results are compared to a conventional carbon fiber-based material (Toray TGP-H-060, abbreviated as T60).

The electronic conductivities σ of the S-PET materials are anisotropic in in-plane and through-plane directions and reflect the thickness of the gold layer (cf. Table 4). In in-plane direction, S-PET-5 exhibits a conductivity of 1.6×10^4 S m⁻¹, which is similar to the conductivity of the T60 carbon paper (1.5×10^4 S m⁻¹) [31,32]. S-PET-1, with only a fifth of the gold thickness, has a 10 times lower conductivity, that is 1.8×10^3 S m⁻¹. For the through-plane direction, S-PET-5 shows a conductivity of 5.5×10^4 S m⁻¹ (higher than in-plane) and S-PET-1 only 5.5×10^2 S m⁻¹. The different ip/tp trends of S-PET-1 and S-PET-5 arise from the different morphology of the gold layer with different thicknesses at the fiber intersections. Fig. 2 a2-3 and b2-3 show different contact points between fibers of the woven GDLs. For the higher sputtered gold thickness some gold accumulation is seen at the fiber junctions, which is not present for the thin coating, leading to the different trends. For the T60 GDL, comprised of around 10 layers of parallel stacked carbon fibers, the lower through-plane-conductivity stems from the contact resistance at these fiber junctions. Overall it can be noted that the S-PET materials have comparable or better electronic conductivities, so the electron transport is not a limiting factor for cell performance.

For the S-PET fabrics, PET forms the vast majority of volume and mass. Therefore, even with its low thermal conductivity (0.24 W m⁻¹ K⁻¹), the polymer contributes to the overall thermal conductivity κ of the composite materials. The thermal conductivity in metals can be deduced with the Wiedemann-Franz law (Eq. (2.1)) from the electronic conductivity, as heat transfer in metals occurs mainly by electron flow [29]. Therefore, the total thermal conductivity was calculated as the sum of the electronic contribution (from the gold layer, Au-100/Au-500) and the phonon contribution (from the PET base fabric PET_S). The effective thermal conductivities of the

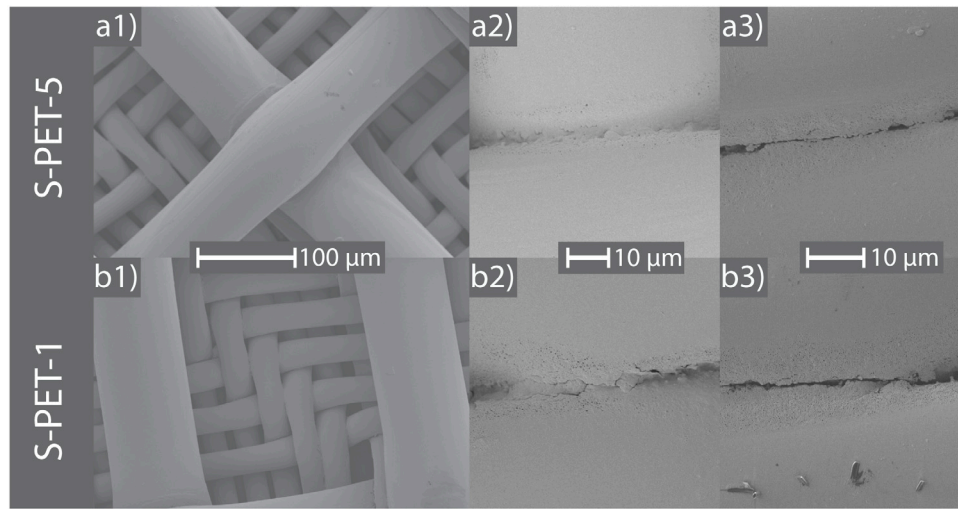


Fig. 2. Gold-coated S-PET-5 GDL with the coarse carrier layer on top. The thick wires have a diameter of 80 μm , the thin fibers 24 μm .

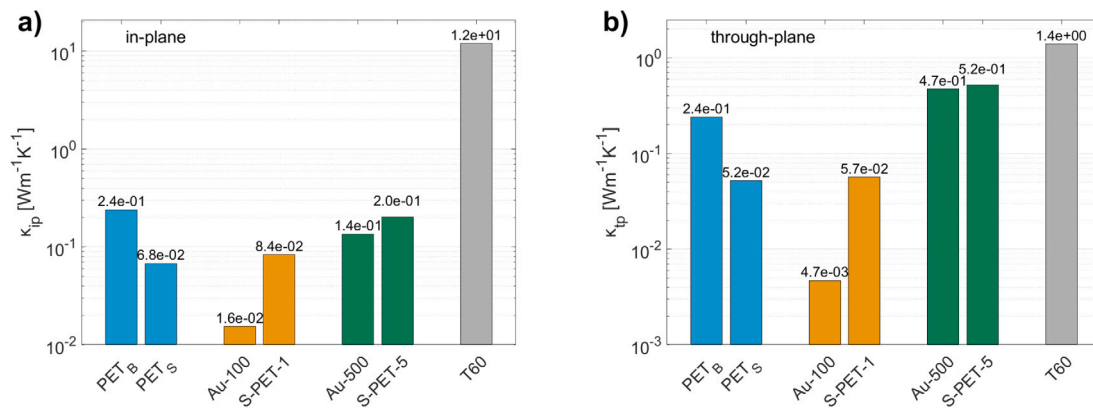


Fig. 3. Thermal conductivities κ in (a) in-plane and (b) through-plane directions for PET (bulk and simulated fabric) and the three GDL materials Au-100/S-PET-1, Au-500/S-PET-5, and T60. The subscripts for PET denote B for the bulk value and S for the GDL structure. The values Au-X00 indicate the purely electronic contribution from the gold coating.

Table 4

Electronic conductivities $\sigma_{ip/ip}$ of the three investigated GDL materials S-PET-1, S-PET-5 and T60 and the corresponding relation to the carbon GDL T60.

| GDL | σ_{ip} [S m ⁻¹] | T60 \times [–] | σ_{ip} [S m ⁻¹] | T60 \times [–] |
|---------|---------------------------------------|---------------------|---------------------------------------|---------------------|
| S-PET-1 | 1.8×10^3 | $\times 0.1$ | 5.5×10^2 | $\times 0.5$ |
| S-PET-5 | 1.6×10^4 | $\times 1.1$ | 5.5×10^4 | $\times 50$ |
| T60 | 1.5×10^4 | $\times 1$ | 1.2×10^4 | $\times 1$ |

PET substrate (shown as PET_S in Fig. 3) were calculated based on tomography obtained structures and the bulk thermal value (PET_B). Fig. 3 shows all κ values in in-plane and through-plane directions for the different GDLs.

These results show, that the thermal conductivity for S-PET-1 in both directions is dominated by the PET substrate and the gold layer makes a minor contribution. S-PET-5 on the other hand, due to its high electronic conductivities, has an electronically dominated κ . However, both materials have a lower thermal conductivity than the carbon fiber-based T60. In the in-plane direction, there is 2 to 3 orders of magnitude difference between T60 and S-PET-5/S-PET-1. In through-plane direction, this factor reduces to roughly 0.4 for S-PET-5 and 0.05 for S-PET-1.

3.2. Electrochemical performance

The GDL's influence on the electrochemical performance is its key property and is discussed first. Oxygen transport resistance is used to quantify the differences between the three GDL materials. The material properties and fuel cell operating conditions are then incorporated in a 2D thermal model (cf. Section 2.3) to calculate the different temperature gradients, based on the different thermal conductivities, in the GDLs. This model is used to analyze the differences in high frequency resistance (HFR) and to discuss the heat and water transport through the three materials (cf. Section 3.4).

3.2.1. Fuel cell polarization

The electrochemical performance of the three GDLs was analyzed in differential cells at low (50 °C) and high (80 °C) operating temperatures under dry (60% RH_C) and wet (100% RH_C) cathode gas humidity conditions, to characterize the influence of the GDL thermal conductivity with different temperature and humidity boundary conditions.

For the polarization curves at cold temperatures, shown in Fig. 4 a and b (50 °C, with a water vapor saturation pressure of 123 mbar), only a low fraction of the product water can be transported through the GDL in the gas phase. The woven GDLs, S-PET-1 and S-PET-5, show stable performance under the dry conditions up to 2.25 A cm⁻² and show only a slight decline in voltage at high current densities. This indicates just a minor increase of the oxygen transport resistance due to

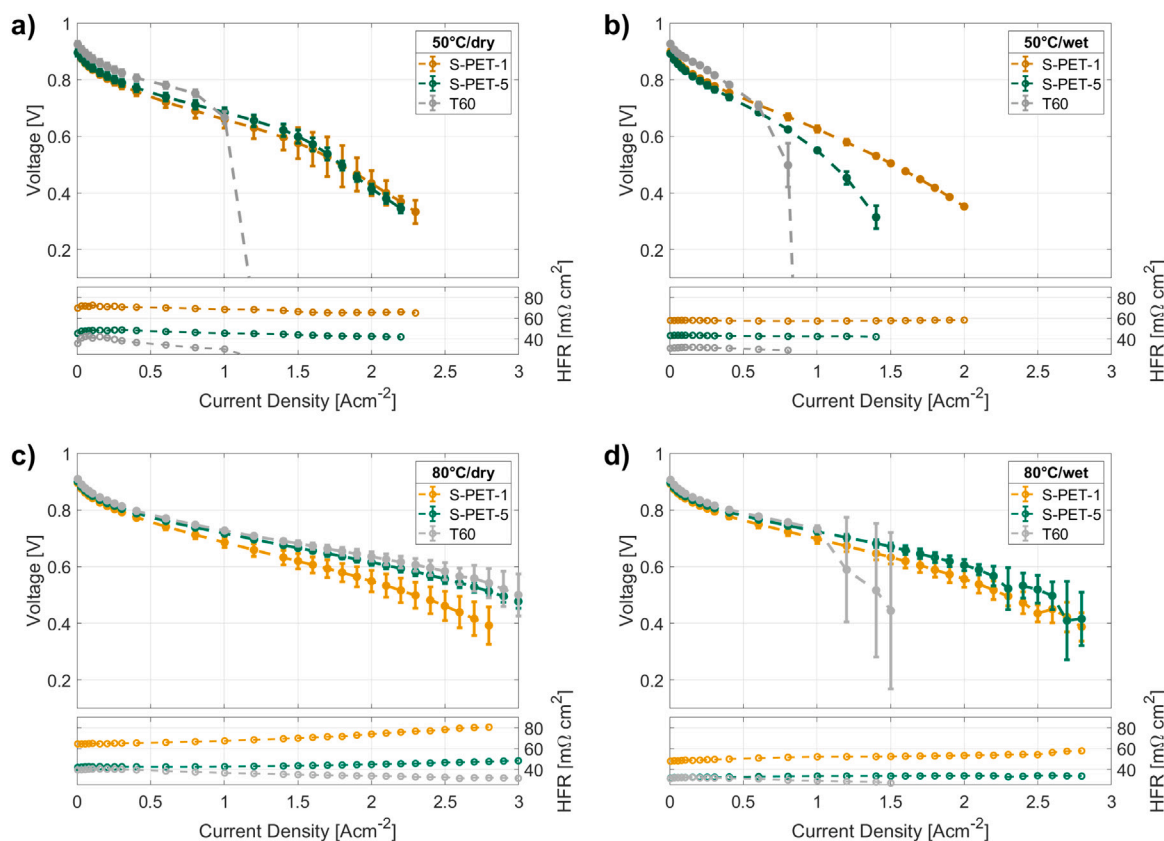


Fig. 4. Polarization curves at (a–b) 50 °C and (c–d) 80 °C of the three investigated GDL materials S-PET-1, S-PET-5, and T60. Figures (a) and (c) show cell voltage behavior at dry cathode conditions (60% RH_C), (b) and (d) at saturated (wet) cathode conditions (100% RH_C). Bottom graphs display the high frequency resistance (HFR). Cells were operated at 150 kPa with H₂/air.

liquid water, attributed to the simple, deterministic structure with just one pore throat between the water generating catalyst layer and gas channels [27]. Both woven fabrics show similar performance, as they have an identical structure for gas and water transport. The difference of an order of magnitude in thermal conductivity does not influence their cell performance.

Under cold and wet conditions, however, the polarization behavior of the two fabric-based GDLs diverges and the effect of the thermal conductivity can be observed. A lower κ results in a larger the temperature gradient between CL (heat source) and flow fields (heat sink). With constant conditions in the flow field, this leads to higher temperatures in membrane, CLs, and GDLs. For S-PET-1, with the lowest thermal conductivity, the higher temperature gradient decreases condensation and thus, reduces the mass transport losses which can be observed for S-PET-5 and T60. However, this also reduces humidity and proton conductivity of the membrane and the resulting almost linear decrease in cell voltage indicates ohmic-dominated overpotentials (cf. *iR* corrected polarization curves in Figure S4). The cell voltage drops rapidly for S-PET-5 above 1 A cm^{-2} , and a clear performance hierarchy between the three GDLs is established. The conventional carbon GDL T60 shows the highest mass transport losses, starting in dry conditions from 1 A cm^{-2} and with wet feed gas at 0.75 A cm^{-2} , limiting the maximum achievable current density. These large mass transport overpotentials are due to the stochastic, random pore space, which is prone to flooding with a slower drainage rate.

The same performance analysis at a high operating temperature of 80 °C is shown in Figs. 4 c and d. The water vapor saturation pressure at this temperature is 474 mbar, 4 times higher than at 50 °C and all (or at least a large fraction) of the product water is transported through the GDL in the gas phase under dry conditions (Figs. 4 c). Therefore, at dry conditions, T60 and S-PET-5 show the same stable performance

up to 3 A cm^{-2} . S-PET-1 exhibits a slightly reduced voltage caused by the increased HFR, as corroborated by the *iR*-corrected polarization curves in Figure S4 c, which are identical. For S-PET-1, the increased HFR can be attributed again to an increased temperature at the membrane and thereby, leading to a reduced water content and membrane conductivity.

The situation changes at wet conditions (cf. Fig. 4 d): the two woven GDLs show a stable performance until $\sim 2.5 \text{ A cm}^{-2}$. The *iR*-corrected performance shows an almost identical voltage behavior for both S-PET-1 and S-PET-5, thus indicating the same water management and transport properties for the identical structures. The conventional stochastic GDL again shows the lowest performance due to flooding, as is shown by the drastically lower current density and unstable operation at higher current densities. The thermal properties and temperature distribution in all materials are discussed in more detail in Section 3.3.

3.2.2. Oxygen transport resistance analysis

The oxygen transport resistance R_{T,O_2} describes the effectiveness of oxygen transport through the pore network from the channel to the reaction sites in the CL. Thus, an increase in R_{T,O_2} can be related to increasing liquid water saturation in the GDL (flooding) of the catalyst layer and/or the GDL and subsequent elongation and blockage of gas paths. The oxygen transport resistance has been determined for all previously described operating conditions, as it is expected that for different thermal GDL conductivities, different liquid saturations evolve, driven by the changing temperature gradients (as all fuel cell assemblies were using the same, commercial CCMS).

Under cold and dry operating conditions (50 °C T_{cell} , 60% RH_A/60% RH_C, cf. Fig. 5 a), the oxygen transport resistance of S-PET based GDLs shows no increase with increasing current density, indicating a fully

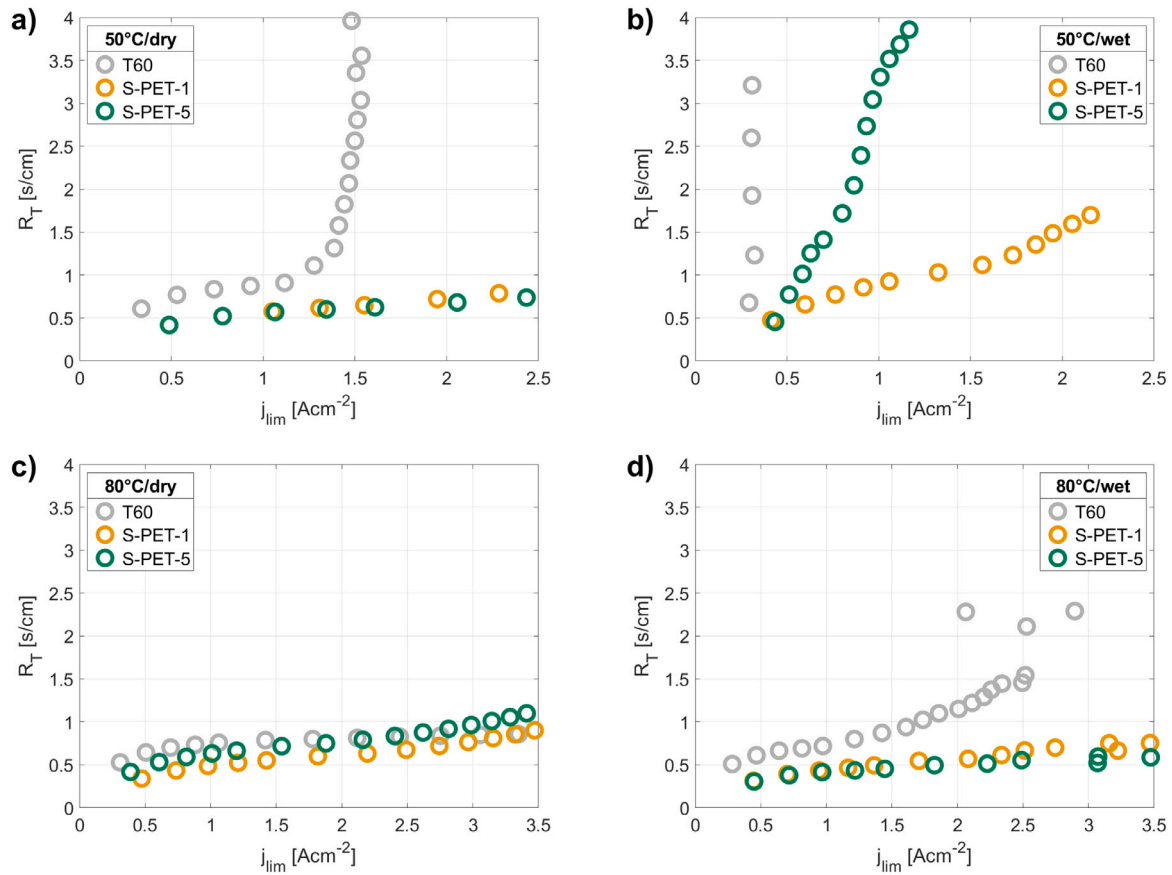


Fig. 5. Oxygen transport resistance R_{T,O_2} at (a)–(b) 50 °C and (c)–(d) 80 °C of the three investigated GDL materials S-PET-1, S-PET-5, and T60. Figures (a) and (c) show R_{T,O_2} at dry conditions (60%RH_A/60% RH_C), (b) and (d) at wet cathode conditions (80%RH_A/95% RH_C). Cells were operated at 150 kPa, H₂, and varying oxygen concentration on the cathode side.

dry structure. Furthermore, already at low current densities, R_{T,O_2} is around 30% lower than for T60. With no liquid water present, the enhanced oxygen transport can be attributed to the different structural properties, i.e. their lower tortuosity and higher effective diffusivity. For the stochastic carbon GDL, a sharp increase in R_{T,O_2} occurs at 1 A cm⁻². This effect indicates flooding of CL and/or GDL, and its onset corresponds well with the onset of mass transport limitations visible in Fig. 4 a.

For cold and wet operating conditions (50 °C T_{cell} , 80% RH_A/95% RH_C, cf. Fig. 5 b), the same order of the three GDL materials is found, being in line with the polarization characteristics. S-PET-1, shows the highest cell voltage and stable operation with a delayed, slow increase in R_{T,O_2} at current densities higher than 1.5 A cm⁻². S-PET-5 shows an earlier and steeper slope, indicating gradually rising water saturation. This supports the hypothesis, that the thermal properties have a distinct influence on the liquid saturation, with higher temperature gradients leading to lower water blockage. T60 shows a nearly vertical R_{T,O_2} increase already at current densities below 0.5 A cm⁻², suggesting that under these conditions, the deterministic GDL structure is as well highly important for fuel cell performance.

At hot and dry conditions (80 °C T_{cell}), almost identical oxygen transport resistance behavior is found for all materials, coinciding well with the polarization curves in Fig. 4 c, where none of the GDL exhibited significant mass transport overpotentials in the investigated current density region. Obviously, and quite naturally, under dry conditions, the thermal conductivity is not a critical GDL parameter.

For the hot and wet conditions the S-PET materials again show minor change in the oxygen transport resistance. Only T60 shows at current densities higher than 1.5 A cm⁻² an increase in R_{T,O_2} (correlating well with Fig. 4 d). Therefore, under these conditions, a factor

of 10 to 100 in thermal conductivity among the materials does not have a significant impact on the liquid saturation dependent transport properties, indicating that thermal conductance of the GDL has a minor influence only at high temperatures. The difference between the S-PET materials and T60 is therefore mainly given by their structure.

3.3. Cathode GDL temperature distribution

The thermal conductivity of the GDL can have a strong influence on the temperature distribution in the cell. To understand the evolving thermal gradients, a 2D model was used to describe the resulting temperature fields for high current density operation with the concurring high heat fluxes. The reaction heat, produced in the cathode catalyst layer is the main heat source. A heat production Q_{ORR} in the cathode catalyst layer of 870 mW cm⁻² (corresponding to a current density of about 1.5 A cm⁻² for the presented cell components) and constant temperature at the backside of the flow field rib (controlled by the cooling circuit of 80 °C) were assumed. Heat flow through the MEA to the anode flow field is also considered, and included as flux boundary at the membrane/aCL interface. For more details see the experimental Section 2.3.

Figs. 6 a–c show the simulated temperature distribution for S-PET-1, S-PET-5, and T60 with the described boundary conditions. S-PET-1 shows significant heat accumulation in the membrane, CL and GDL, which is caused by its very low through-plane thermal conductivity (κ_{tp} 20x lower than T60). The temperature in the catalyst layer, membrane, and GDL reaches locally more than 100 °C, and an average catalyst and membrane temperature above 98 °C was calculated (cf. Table S1). S-PET-5 (cf. Fig. 6 b), due to the higher κ_{tp} , transports the reaction heat better away, reaching maximum temperatures of only 85 °C, and

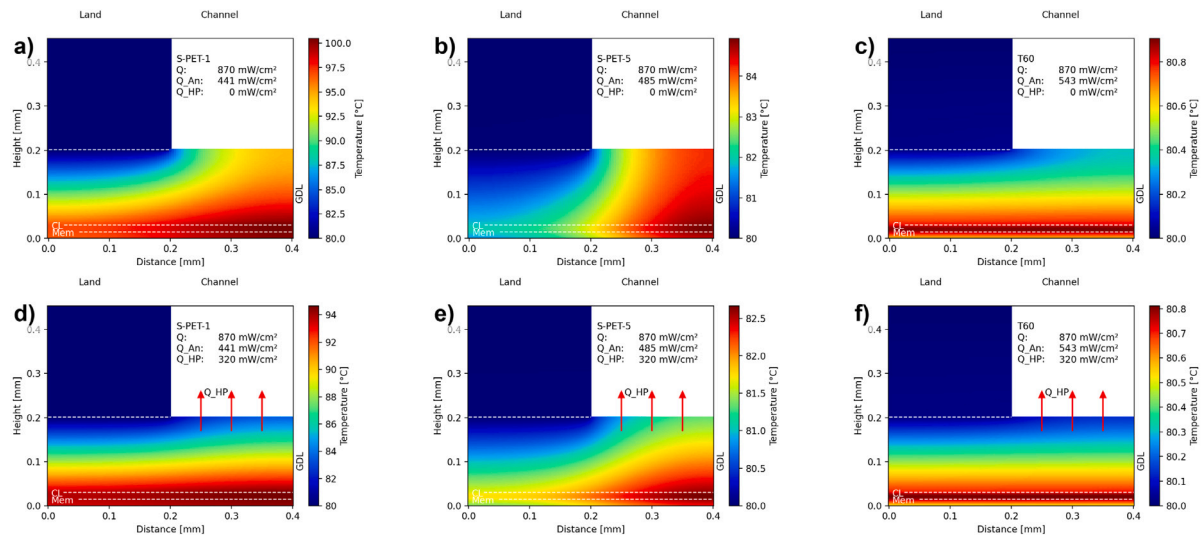


Fig. 6. (a)–(c) Simulated 2D steady-state temperature distributions of the three investigated GDLs, assuming a heat production of $Q_{ORR} = 870 \text{ mW cm}^{-2}$ in the cathode catalyst layer and a constant flow field temperature of 80°C in both anode and cathode flow fields; (d)–(f) Simulated 2D steady-state temperature distributions including cooling by the heat-pipe effect, assuming total evaporation of all product water at 1.5 A cm^{-2} , resulting in a cooling power of $Q_{HP} = 320 \text{ mW cm}^{-2}$ reaching the channel.

average membrane and CL temperatures of 83°C . Due to its anisotropic thermal conductivity, the temperature gradient is most pronounced in the in-plane direction and thus leads to lower catalyst temperatures below the rib than at the channel ($\Delta T = 3^\circ\text{C}$). Still, the temperature in the cell is higher than for the carbon GDL T60 (cf. Fig. 6 c). The superior thermal conductivity of carbon transmits the waste heat fast towards the flow field and thus it exhibits the lowest temperature gradient in the simulated assembly.

The calculated temperature gradient in the woven GDLs is large enough to drive a heat pipe cooling effect, where product water is evaporated at the catalyst layer and transported to the channel in the vapor phase [39–42]. The maximum cooling potential via the heat pipe effect was estimated assuming complete evaporation of product water at 1.5 A cm^{-2} . This gives a cooling power Q_{HP} of 320 mW cm^{-2} , which was implemented as outgoing heat flux into the channel at the GDL/channel interface (assuming no prior condensation in the GDL). This additional cooling power changes the temperature distribution significantly for S-PET-1, as is shown in Fig. 6 d. The temperature at the membrane and catalyst layer was reduced by 6°C , and the high temperatures observed in the GDL, CL and membrane below the channel are reduced. Membrane drying and degradation at these elevated temperatures could be exacerbated which could in-turn affect the cell durability and lifetime. This is an important factor which should be considered when designing GDLs with low thermal conductivities. The GDL temperature at the channel interface is still at around 84°C . Thus, the assumption of no condensation inside the structure (considering the high stoichiometric flow rates used for the differential cell) appears to be valid. For S-PET-5, with its 10 times higher through-plane thermal conductivity κ_{tp} , the heat pipe cools the GDL less, as can be seen from Fig. 6 e. Still, a 2°C reduction can be achieved in the CL and membrane, and the GDL/channel interface temperature is also, reduced by 1.5°C . Including the heat-pipe cooling flux for the carbon GDL has a negligible impact on the temperature distribution (cf. Fig. 6 f). The temperature gradient is already too low in the base case (no heat pipe effect) to drive a significant heat pipe through the GDL [43].

3.4. High-frequency resistance analysis

The high frequency resistance (HFR) includes contributions from contact resistances, electronic bulk resistances, and the proton resistance of membrane and ionomer. Thus it contains important information on the current membrane hydration level, which can be correlated

Table 5

High frequency resistance (HFR) at 1.5 A cm^{-2} (or the maximum current density above 0.5 V) of the three GDL materials S-PET-1, S-PET-5, and T60 at cold and hot temperatures ($50^\circ\text{C}/80^\circ\text{C}$) and dry and wet cathode gas channel conditions ($60\% \text{ RH}_C/100\% \text{ RH}_C$).

| T_{cell} [$^\circ\text{C}$] | RH_C [%] | S-PET-1 [$\text{m}\Omega \text{ cm}^2$] | (ΔT_{60}) [%] | S-PET-5 [$\text{m}\Omega \text{ cm}^2$] | (ΔT_{60}) [%] | T60 [$\text{m}\Omega \text{ cm}^2$] |
|------------------------------------|----------------------|----------------------------------------------|----------------------------|----------------------------------------------|----------------------------|------------------------------------------|
| 50 | 60 | 69 | 121 | 46 | 47 | 31 |
| 50 | 100 | 57 | 91 | 42 | 41 | 30 |
| 80 | 60 | 67 | 84 | 43 | 17 | 37 |
| 80 | 100 | 52 | 80 | 34 | 15 | 29 |

to the membrane temperature. The overall HFR of cells with the three GDLs is summarized for all operating conditions in Table 5. S-PET-1 shows for all operating conditions a 70%–100% increased HFR as compared to the carbon GDL T60, with the lowest recorded resistance. S-PET-5 exhibits a slightly increased HFR, that is lowest at 80°C and 100% RH_C .

To split the single contributions to the overall HFR, the contact resistances were approximated from literature values (Makharia et al.) for a similar Toray GDL/Nafion membrane combination, summing up to $16.4 \text{ m}\Omega \text{ cm}^2$ [16]. The measured and calculated electronic bulk resistances for the GDL materials were below $3.3 \text{ m}\Omega \text{ cm}^2$ (reached for S-PET-1 with the lowest σ_{tp} , cf. Figure S1 a).

Although electronic contact and bulk resistances do not change with varied operating conditions such as temperature T_{cell} or cathode gas humidity RH_C , the membrane resistance is strongly dependent on the local humidity [44]. Furthermore, the contribution from the membrane is 4 times higher with $12.5 \text{ m}\Omega \text{ cm}^2$ at 100% RH and 80°C . Even with the maximum heat pipe cooling, the temperature at the CL for S-PET-1 is 14°C higher than at the flow field, to which the relative humidity in the gas channels was set. Therefore, the relative humidity (100% RH_C in the channel, corresponding to a dew-point of 80°C DP_C), is significantly reduced at CL and membrane. The average membrane temperature from the simulations including the heat pipe effect was used to recalculate the relative humidity at the membrane RH_{mem} and its corresponding resistance. Together with the contributions from contact and GDL bulk resistance, the overall expected HFR was calculated and is compared in Fig. 7 to the measured values.

At wet conditions, (80°C , DP_C , cf. Fig. 7 a), the calculated values coincide well with the measured HFR for all three materials. This strongly supports the hypothesized heat pipe effect for the woven GDLs, as the

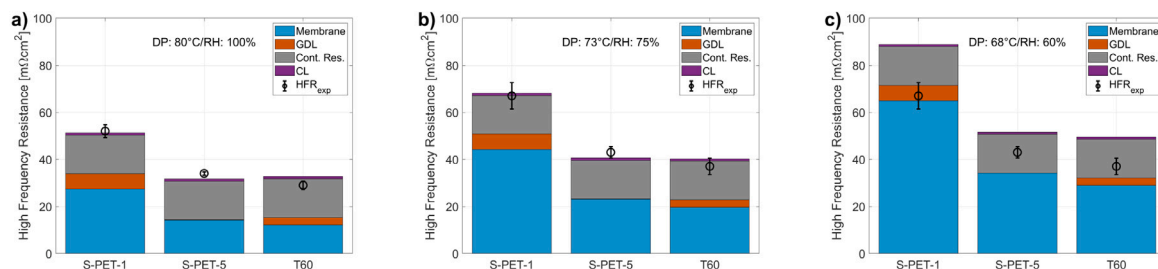


Fig. 7. Calculated high frequency resistance (HFR) of cells with different GDLs, accounting for the simulated, increased membrane temperature and thereby changed membrane resistance for dew-points of (a) 80 °C (100% RH_C) (b) 73 °C (70% RH_C) and (c) 68 °C (60% RH_C).

calculated change in temperature accurately describes the increased membrane resistance at these operating conditions (cf. Fig. 4 and Table 5). Only for S-PET-5, a slight deviation of 2.5 mΩ cm² is observed, which would indicate a slightly higher membrane temperature (and lower RH_{mem}). This can be explained by an over-estimation of the heat pipe cooling for this material. Due to the lower temperature gradient of +5 °C it is expected, that the heat pipe contributes to the conductive heat transport, but is not as developed (i.e. $Q_{HP} < 320 \text{ mW cm}^{-2}$) as for the S-PET-1 GDL.

At lower gas dew points of 68 °C DC_C (corresponding to 60% RH_C, cf. Fig. 7 c), a larger offset is calculated for all materials, and the membrane resistance overestimated. However, two contributions can increase the membrane humidity and thus reduce the estimated resistance: cross-membrane water flow from the anode side, and locally remaining product water. The humidity of the anode gas stream (RH_A) was constantly at 80%. Therefore, the overall membrane humidity can be expected to be higher than 60%. Secondly, produced water can also humidify the membrane instead of being evaporated and transported to the cathode gas channel. This effect would however reduce the heat pipe cooling power and thus partially counteracts a higher membrane conductivity. Figure S5 shows the dependence of the HFR and the estimated membrane dew-point for the three materials. For S-PET-1 this indicates a RH_{mem} at the membrane of around 75%/ 73 °C DP_{mem}, that can also explain the HFR contributions for the other two materials well (cf. Fig. 7 b). In general, the sensitivity of the membrane on humidity changes is reduced for S-PET-5 and T60, as the developed temperature gradients are much smaller for these cases.

3.5. Heat & water transfer mechanisms

In GDLs, heat and water transfer are closely connected. S-PET-1 and S-PET-5, with the identical structure, show stable and similar fuel cell performance in most conditions. The only differences are found in cold & wet, and hot & dry conditions, where the 10x times lower thermal conductivity of S-PET-1 makes the difference. However both deterministic GDLs significantly reduce mass transport overpotentials as compared to T60 at saturated conditions, regardless of the operating temperature (Fig. 5). The different suggested water transport mechanisms through the three investigated GDL materials are illustrated in Fig. 8 and discussed below. The lower GDL thermal conductivity causes higher catalyst layer temperatures and an RH gradient, as is also reported by other authors [45]. This temperature gradient enables a heat pipe effect, that not only cools the cell, but also positively impacts water transport. At cold conditions (50 °C), S-PET-1 heats up by more than 10 °C and thus, significantly increases the water vapor saturation pressure and evaporation. Therefore, most product water can be transported as vapor to the channel in both dry and wet conditions (100% RH_C). Part of the product water remains in the membrane and ionomer, which can be seen, for example, in the stable HFR of Fig. 4 a and b, controlling the ohmic losses of this material (cf. Fig. 8 a). S-PET-5 (at a lower GDL temperature then S-PET-1), shows an identical performance under cold and dry conditions. Again, most of the water is transported in the gas phase and the remaining, liquid

product water is efficiently drained to the channels. Under cold and wet conditions, the liquid water saturation in the GDL increases due to condensation, increasing the oxygen transport resistance and reducing the cell voltage (cf. Figs. 4 b and 5 b). Therefore, S-PET-1 performs the best at these conditions due to the proposed heat pipe effect. At low temperatures of 50 °C (regardless of the gas channel humidity), T60 has the worst performance due to mass transport limitations caused by water accumulation in its stochastic pore space (cf. Fig. 8 a).

For operation under hot and dry conditions, all product water can be transported in the gas phase and thus, all three materials show a similar performance. However, the high temperature gradient observed in the S-PET-1 GDL dries the membrane and therefore, this material shows the highest ohmic losses and a slightly reduced cell voltage. With an increase in the humidity of the feed gas during wet operation, this drying effect is reduced by a higher fraction of liquid product water which humidifies membrane and ionomer. Thus, S-PET-1 and S-PET-5 show almost identical performance, which is related to their simple, two-layered structure. This observation is contrary to previous studies, that used GDLs with different structures and different κ (e.g. Owejan et al.), or simulated GDLs with different thermal conductivities (e.g. Zhou et al.) and observed much higher performance differences between their materials [45,46]. Our results indicate that the influence of the thermal conductivity was overestimated. Some problems of water management such as liquid water condensation and saturation close to the catalyst layer can be resolved also with the simpler, two-dimensional structure which is open to the channel.

Still we conclude, that a lower thermal conductivity (than e.g. T60) is necessary and highly beneficial, as it enables the heat pipe and increases vapor phase transport. This heat pipe is partially self-regulating, as it becomes more pronounced with lower κ . (cf. Fig. 7a, Fig. 8b). Even with just 2% of the thermal conductivity of T60, S-PET-1 still shows a remarkable fuel cell performance. S-PET-5, with 40% of $\kappa_{tp,T60}$, exhibits only a 2 °C higher temperature compared to T60. This material still decreases mass transport losses as compared to the stochastic material and exhibits superior performance at most of the investigated operating conditions.

4. Conclusions and outlook

The presented study used a bottom-up approach to design GDL materials with different thermal conductivities retaining an identical structure, so the influence of the thermal properties can be studied without cross-effects of different structures. This unique property was used to compare the performance of two woven GDL materials (S-PET-1 and S-PET-5) with identical structure but an order of magnitude different thermal conductivity.

The woven fabrics have a simple, two-layered design, that comprises only one layer of pore throats and leads to an efficient water transport, as reported before. The higher temperature gradient for low- κ GDLs drives a partially self-regulating heat pipe effect, which not only enhances vapor phase water transport but also cools the cell. Thus, both S-PET materials with largely different thermal conductivities exhibit similar performance at most operating conditions, surpassing

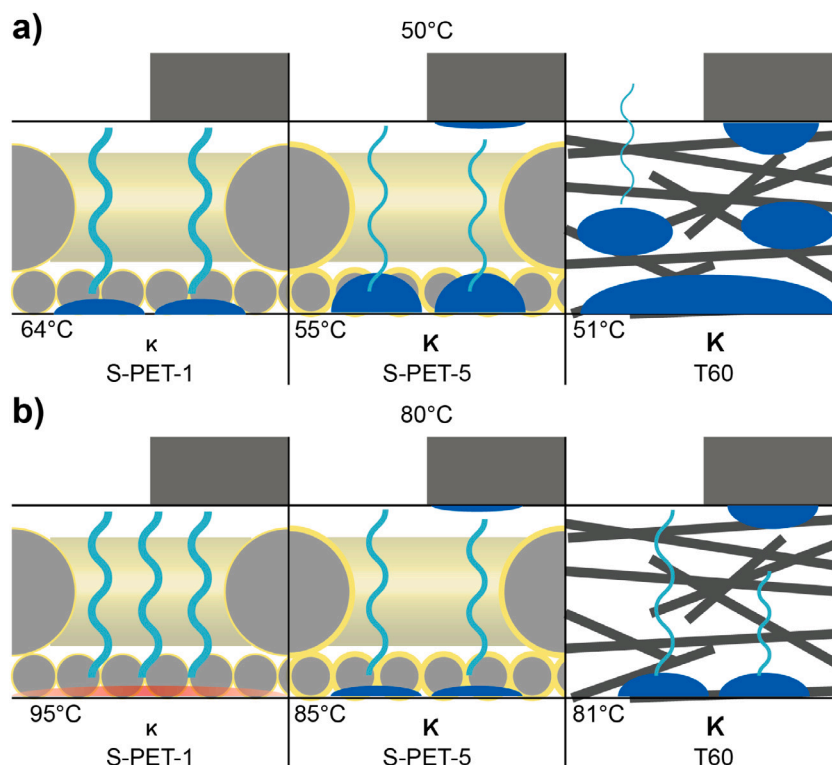


Fig. 8. Illustration of water transport and accumulation through the three different GDLs in (a) cold (50 °C) and (b) hot (80 °C) conditions. Dark blue droplets indicate liquid water, the light blue lines water vapor. (For interpretation of the references to color in this figure legend, the reader is referred to the web version of this article.)

the performance of a conventional carbon GDL (with $\kappa_{ip,T60}$ close to S-PET-5). This stands partially in contrast to previous studies, where the role of the thermal conductivity was overestimated and no effect of the GDL microstructure was proposed. Therefore, the thermal conductivity alone should not be the decisive criterion for future GDL materials. Still, heat and water transport are tightly connected by the proposed heat pipe effect: lower thermal conductivity increases vapor phase transport, enables the proposed heat pipe effect, and causes the difference at cold and wet operating conditions.

Commercial fuel cells include an MPL on top of the GDL, that is hypothesized to improve performance under wet conditions due to a similar heat pipe effect, but also, introduces a new diffusion barrier, increasing mass transport losses under dry conditions. Based on the results of this paper we hypothesize, that optimizing the thermal conductivity and the structure of the woven GDLs could be functionally equivalent to commercial GDLs with hydrophobic MPLs while reducing the diffusion length and hence, mass transport losses.

CRediT authorship contribution statement

Christoph Csoklich: Investigation, Formal analysis, Validation, Visualization, Writing – original draft. **Mayank Sabharwal:** Methodology, Software, Formal analysis, Writing – review & editing. **Thomas J. Schmidt:** Conceptualization, Resources, Supervision, Writing – review & editing. **Felix N. Büchi:** Conceptualization, Supervision, Funding acquisition, Project administration, Resources, Writing – review & editing.

Declaration of competing interest

The authors declare that they have no known competing financial interests or personal relationships that could have appeared to influence the work reported in this paper.

Acknowledgments

The authors thank the Swiss Federal Office of Energy for funding this project. Furthermore, Dr. Jens Eller and his highly appreciated input on the heat pipe effect, Dr. Roland Steim and SEFAR for the provision of materials, and Thomas Gloor for technical support are gratefully acknowledged, as well as Dr. Michael Striednig and Arnaud Schuller for ideas and discussions.

This project was funded under the grant SI/501635-01 from the Swiss Federal Office of Energy.

Supporting information

Supplementary material related to this article can be found online at <https://doi.org/10.1016/j.jpowsour.2022.231539>.

References

- [1] I. Staffell, D. Scamman, A. Velazquez Abad, P. Balcombe, P.E. Dodds, P. Ekins, N. Shah, K.R. Ward, The role of hydrogen and fuel cells in the global energy system, *Energy Environ. Sci.* 12 (2) (2019) 463–491.
- [2] M. Ball, M. Weeda, The hydrogen economy - vision or reality? *Int. J. Hydrogen Energy* 40 (25) (2015) 7903–7919.
- [3] I. Staffell, Stationary fuel cells - residential applications, in: *Fuel Cells : Data, Facts and Figures*, in: Wiley Online Books, Weinheim, Germany, 2016, pp. 282–292, <http://dx.doi.org/10.1002/9783527693924.ch29>.
- [4] R.C. Samsun, Global development status of fuel cell vehicles, in: *Fuel Cells : Data, Facts and Figures*, in: Wiley Online Books, Wiley-VCH Verlag GmbH & Co. KGaA., 2016, pp. 37–60, <http://dx.doi.org/10.1002/9783527693924.ch05>.
- [5] M. Robinius, A. Otto, P. Heuser, L. Welder, K. Syranidis, D. Ryberg, T. Grube, P. Markewitz, R. Peters, D. Stolten, Linking the power and transport sectors—Part 1: The principle of sector coupling, *Energies* 10 (7) (2017) 956.
- [6] T.M. Gür, Review of electrical energy storage technologies, materials and systems: Challenges and prospects for large-scale grid storage, *Energy Environ. Sci.* 11 (10) (2018) 2696–2767.
- [7] S.T. Thompson, B.D. James, J.M. Huya-Kouadio, C. Houchins, D.A. DeSantis, R. Ahluwalia, A.R. Wilson, G. Kleen, D. Papageorgopoulos, Direct hydrogen fuel cell electric vehicle cost analysis: System and high-volume manufacturing description, validation, and outlook, *J. Power Sources* 399 (August) (2018) 304–313.

- [8] A. Ajanovic, R. Haas, Economic and environmental prospects for battery electric and fuel cell vehicles: A review, *Fuel Cells* 19 (5) (2019) 515–529.
- [9] U.S. Department of Energy, Multiyear research, development and demonstration plan, Technical Report, Office of Energy Efficiency & Renewable Energy, 2012, <http://dx.doi.org/10.2172/1219578>.
- [10] Z.P. Cano, D. Banham, S. Ye, A. Hintennach, J. Lu, M. Fowler, Z. Chen, Batteries and fuel cells for emerging electric vehicle markets, *Nature Energy* 3 (4) (2018) 279–289.
- [11] T. Suzuki, A. Iiyama, N. Kubo, N. Saito, K. Shinohara, S. Shimotori, Y. Sugawara, K. Yamada, (Invited) toward the future fuel cell -challenge for 2040, *ECS Trans.* 92 (8) (2019) 3–7.
- [12] N. Konno, S. Mizuno, H. Nakaji, Y. Ishikawa, Development of compact and high-performance fuel cell stack, *SAE Int. J. Alternat. Powertrains* 4 (1) (2015) 123–129.
- [13] S. Neatu, F. Neatu, I.M. Chirica, I. Borbáth, E. Tálas, A. Tompos, S. Somacescu, P. Osiceanu, M.A. Folgado, A.M. Chaparro, M. Florea, Recent progress in electrocatalysts and electrodes for portable fuel cells, *J. Mater. Chem. A* 9 (32) (2021) 17065–17128.
- [14] K.C. Neyerlin, W. Gu, J. Jorne, H.A. Gasteiger, Determination of catalyst unique parameters for the oxygen reduction reaction in a PEMFC, *J. Electrochem. Soc.* 153 (10) (2006) A1955.
- [15] K.C. Neyerlin, W. Gu, J. Jorne, H.A. Gasteiger, Study of the exchange current density for the hydrogen oxidation and evolution reactions, *J. Electrochem. Soc.* 154 (7) (2007) B631.
- [16] R. Makharia, M.F. Mathias, D.R. Baker, Measurement of catalyst layer electrolyte resistance in PEMFCs using electrochemical impedance spectroscopy, *J. Electrochem. Soc.* 152 (5) (2005) A970.
- [17] T. Kotaka, O. Aoki, T. Shiomi, Y. Fukuyama, N. Kubo, Y. Tabuchi, The influence of micro structure of the GDL and MPL on the mass transport in PEMFC, *ECS Trans.* 41 (1) (2011) 439–448.
- [18] M.M. Mench, Performance characterization of fuel cell systems, in: *Fuel Cell Engines*, in: Wiley Online Books, John Wiley & Sons, Inc., 2008, pp. 121–190, <http://dx.doi.org/10.1002/9780470209769.ch4>.
- [19] M.F. Mathias, J. Roth, J. Fleming, W. Lehnert, Diffusion media materials and characterisation, in: *Handbook of Fuel Cells*, Vol. 3, John Wiley & Sons, Ltd, Chichester, UK, 2010, pp. 517–537, <http://dx.doi.org/10.1002/9780470974001.f303046>, <https://onlinelibrary.wiley.com/doi/10.1002/9780470974001.f303046>.
- [20] I.V. Zenyuk, D.Y. Parkinson, L.G. Connolly, A.Z. Weber, Gas-diffusion-layer structural properties under compression via X-ray tomography, *J. Power Sources* 328 (2016) 364–376.
- [21] D. Niblett, A. Mularczyk, V. Niasar, J. Eller, S. Holmes, Two-phase flow dynamics in a gas diffusion layer - gas channel - microporous layer system, *J. Power Sources* 471 (2020) 228427.
- [22] P. Oberholzer, P. Boillat, Local characterization of PEMFCs by differential cells: Systematic variations of current and asymmetric relative humidity, *J. Electrochem. Soc.* 161 (1) (2014) F139–F152.
- [23] L. Holzer, O. Pecho, J. Schumacher, P. Marmet, O. Stenzel, F. Büchi, A. Lamibrac, B. Münch, Microstructure-property relationships in a gas diffusion layer (GDL) for polymer electrolyte fuel cells, part I: effect of compression and anisotropy of dry GDL, *Electrochim. Acta* 227 (2017) 419–434.
- [24] D. Gerteisen, T. Heilmann, C. Ziegler, Enhancing liquid water transport by laser perforation of a GDL in a PEM fuel cell, *J. Power Sources* 177 (2) (2008) 348–354.
- [25] A. Forner-Cuenca, J. Biesdorf, L. Gubler, P.M. Kristiansen, T.J. Schmidt, P. Boillat, Engineered water highways in fuel cells: Radiation grafting of gas diffusion layers, *Adv. Mater.* 27 (41) (2015) 6317–6322.
- [26] C. Csoklich, T.J. Schmidt, F.N. Büchi, High performance gas diffusion layers with added deterministic structures, *Energy Environ. Sci.* 15 (2022) 1293–1306.
- [27] C. Csoklich, R. Steim, F. Marone, T.J. Schmidt, F.N. Büchi, Gas diffusion layers with deterministic structure for high performance polymer electrolyte fuel cells, *ACS Appl. Mater. Interfaces* 13 (8) (2021) 9908–9918.
- [28] H. Xu, M. Bührer, F. Marone, T.J. Schmidt, F.N. Büchi, J. Eller, F.N. Büchi, J. Eller, Effects of gas diffusion layer substrates on PEMFC water management: Part I. Operando liquid water saturation and gas diffusion properties, *J. Electrochem. Soc.* 168 (7) (2021) 074505.
- [29] W. Demtröder, *Experimentalphysik 1 Mechanik Und Wärme*, seventh ed., Springer-Lehrbuch, Springer Spektrum, Berlin, Heidelberg, Heidelberg, 2015, <http://dx.doi.org/10.1007/978-3-642-25466-6>.
- [30] C. Simon, F. Hasché, H.A. Gasteiger, Influence of the gas diffusion layer compression on the oxygen transport in PEM fuel cells at high water saturation levels, *J. Electrochem. Soc.* 164 (6) (2017) F591–F599, <http://dx.doi.org/10.1149/2.0691706jes>.
- [31] N. Zamel, X. Li, J. Shen, Numerical estimation of the effective electrical conductivity in carbon paper diffusion media, *Appl. Energy* 93 (2012) 39–44.
- [32] J. Becker, R. Flückiger, M. Reum, F.N. Büchi, F. Marone, M. Stamparoni, Determination of material properties of gas diffusion layers: Experiments and simulations using phase contrast tomographic microscopy, *J. Electrochem. Soc.* 156 (10) (2009) B1175.
- [33] N. Zamel, E. Litovsky, S. Shakhshir, X. Li, J. Kleiman, Measurement of in-plane thermal conductivity of carbon paper diffusion media in the temperature range of -20°C to +120°C, *Appl. Energy* 88 (9) (2011) 3042–3050.
- [34] N. Zamel, E. Litovsky, X. Li, J. Kleiman, Measurement of the through-plane thermal conductivity of carbon paper diffusion media for the temperature range from -50 to +120 °C, *Int. J. Hydrogen Energy* 36 (19) (2011) 12618–12625.
- [35] J.G. Pharoah, O.S. Burheim, On the temperature distribution in polymer electrolyte fuel cells, *J. Power Sources* 195 (16) (2010) 5235–5245.
- [36] M. Khandelwal, M. Mench, Direct measurement of through-plane thermal conductivity and contact resistance in fuel cell materials, *J. Power Sources* 161 (2) (2006) 1106–1115.
- [37] P.K. Sinha, C.Y. Wang, Pore-network modeling of liquid water transport in gas diffusion layer of a polymer electrolyte fuel cell, *Electrochim. Acta* 52 (28) (2007) 7936–7945.
- [38] S. Kim, M. Khandelwal, C. Chacko, M.M. Mench, Investigation of the impact of interfacial delamination on polymer electrolyte fuel cell performance, *J. Electrochem. Soc.* 156 (1) (2009) B99.
- [39] A.Z. Weber, J. Newman, Coupled thermal and water management in polymer electrolyte fuel cells, *J. Electrochem. Soc.* 153 (12) (2006) A2205.
- [40] Y. Wang, C.-Y. Wang, A nonisothermal, two-phase model for polymer electrolyte fuel cells, *J. Electrochem. Soc.* 153 (6) (2006) A1193.
- [41] S. Basu, C.-Y. Wang, K.S. Chen, Phase change in a polymer electrolyte fuel cell, *J. Electrochem. Soc.* 156 (6) (2009) B748.
- [42] Y. Wang, K.S. Chen, Through-plane water distribution in a polymer electrolyte fuel cell: Comparison of numerical prediction with neutron radiography data, *J. Electrochem. Soc.* 157 (12) (2010) B1878.
- [43] U. Pasaogullari, P.P. Mukherjee, C.-Y. Wang, K.S. Chen, Anisotropic heat and water transport in a PEMFC cathode gas diffusion layer, *J. Electrochem. Soc.* 154 (8) (2007) B823.
- [44] A. Kusoglu, A.Z. Weber, New insights into perfluorinated sulfonic-acid ionomers, *Chem. Rev.* 117 (3) (2017) 987–1104.
- [45] J.P. Owejan, J.E. Owejan, W. Gu, T.A. Trabold, T.W. Tighe, M.F. Mathias, Water transport mechanisms in PEMFC gas diffusion layers, *J. Electrochem. Soc.* 157 (10) (2010) B1456.
- [46] J. Zhou, S. Shukla, A. Putz, M. Secanell, Analysis of the role of the microporous layer in improving polymer electrolyte fuel cell performance, *Electrochim. Acta* 268 (2018) 366–382.